Scattering phase function spectrum makes reflectance spectrum measured from Intralipid phantoms and tissue sensitive to the device detection geometry

S. C. Kanick,[1,*] V. Krishnaswamy,[1] U. A. Gamm,[2] H. J. C. M. Sterenborg,[2] D. J. Robinson,[2] A. Amelink,[2] and B. W. Pogue[1]

[1]*Thayer School of Engineering, Dartmouth College, 14 Engineering Drive, Hanover, NH 03755, USA.*
[2]*Center of Optical Diagnostics and Therapy, Department of Radiation Oncology, Erasmus Medical Center, PO Box 2040, 3000 CA Rotterdam, The Netherlands.*
*stephen.c.kanick@dartmouth.edu

Abstract: Reflectance spectra measured in Intralipid (IL) close to the source are sensitive to wavelength-dependent changes in reduced scattering coefficient (μ_s') and scattering phase function (PF). Experiments and simulations were performed using device designs with either single or separate optical fibers for delivery and collection of light in varying concentrations of IL. Spectral reflectance is not consistently linear with varying IL concentration, with PF-dependent effects observed for single fiber devices with diameters smaller than ten transport lengths and for separate source-detector devices that collected light at less than half of a transport length from the source. Similar effects are thought to be seen in tissue, limiting the ability to quantitatively compare spectra from different devices without compensation.

© 2012 Optical Society of America

OCIS codes: (170.3660) Light propagation in tissues; (170.7050) Turbid media; (170.6510) Spectroscopy, tissue diagnostics.

References and Links

1. A. Amelink, O. P. Kaspers, H. J. C. M. Sterenborg, J. E. van der Wal, J. L. N. Roodenburg, and M. J. H. Witjes, "Non-invasive measurement of the morphology and physiology of oral mucosa by use of optical spectroscopy," Oral Oncol. **44**(1), 65–71 (2008).
2. J. Q. Brown, K. Vishwanath, G. M. Palmer, and N. Ramanujam, "Advances in quantitative UV-visible spectroscopy for clinical and pre-clinical application in cancer," Curr. Opin. Biotechnol. **20**(1), 119–131 (2009).
3. J. R. Mourant, A. H. Hielscher, A. A. Eick, T. M. Johnson, and J. P. Freyer, "Evidence of intrinsic differences in the light scattering properties of tumorigenic and nontumorigenic cells," Cancer **84**(6), 366–374 (1998).
4. K. Sokolov, M. Follen, and R. Richards-Kortum, "Optical spectroscopy for detection of neoplasia," Curr. Opin. Chem. Biol. **6**(5), 651–658 (2002).
5. I. J. Bigio and S. G. Bown, "Spectroscopic sensing of cancer and cancer therapy: current status of translational research," Cancer Biol. Ther. **3**(3), 259–267 (2004).
6. P. B. Garcia-Allende, V. Krishnaswamy, P. J. Hoopes, K. S. Samkoe, O. M. Conde, and B. W. Pogue, "Automated identification of tumor microscopic morphology based on macroscopically measured scatter signatures," J. Biomed. Opt. **14**(3), 034034 (2009).
7. R. Weersink, M. S. Patterson, K. Diamond, S. Silver, and N. Padgett, "Noninvasive measurement of fluorophore concentration in turbid media with a simple fluorescence /reflectance ratio technique," Appl. Opt. **40**(34), 6389–6395 (2001).
8. M. G. Müller, I. Georgakoudi, Q. Zhang, J. Wu, and M. S. Feld, "Intrinsic fluorescence spectroscopy in turbid media: disentangling effects of scattering and absorption," Appl. Opt. **40**(25), 4633–4646 (2001).
9. S. C. Kanick, D. J. Robinson, H. J. C. M. Sterenborg, and A. Amelink, "Semi-empirical model of the effect of scattering on single fiber fluorescence intensity measured on a turbid medium," Biomed. Opt. Express **3**(1), 137–152 (2012).
10. B. W. Pogue and M. S. Patterson, "Review of tissue simulating phantoms for optical spectroscopy, imaging and dosimetry," J. Biomed. Opt. **11**(4), 041102 (2006).

11. D. A. Boas, A. M. Dale, and M. A. Franceschini, "Diffuse optical imaging of brain activation: approaches to optimizing image sensitivity, resolution, and accuracy," Neuroimage **23**(Suppl 1), S275–S288 (2004).
12. T. O. McBride, B. W. Pogue, E. D. Gerety, S. B. Poplack, U. L. Osterberg, and K. D. Paulsen, "Spectroscopic diffuse optical tomography for the quantitative assessment of hemoglobin concentration and oxygen saturation in breast tissue," Appl. Opt. **38**(25), 5480–5490 (1999).
13. J. R. Mourant, T. Fuselier, J. Boyer, T. M. Johnson, and I. J. Bigio, "Predictions and measurements of scattering and absorption over broad wavelength ranges in tissue phantoms," Appl. Opt. **36**(4), 949–957 (1997).
14. P. Thueler, I. Charvet, F. Bevilacqua, M. St. Ghislain, G. Ory, P. Marquet, P. Meda, B. Vermeulen, and C. Depeursinge, "*In vivo* endoscopic tissue diagnostics based on spectroscopic absorption, scattering, and phase function properties," J. Biomed. Opt. **8**(3), 495–503 (2003).
15. A. Amelink and H. J. C. M. Sterenborg, "Measurement of the local optical properties of turbid media by differential path-length spectroscopy," Appl. Opt. **43**(15), 3048–3054 (2004).
16. M. Johns, C. A. Giller, D. C. German, and H. Liu, "Determination of reduced scattering coefficient of biological tissue from a needle-like probe," Opt. Express **13**(13), 4828–4842 (2005).
17. R. Reif, O. A'Amar, and I. J. Bigio, "Analytical model of light reflectance for extraction of the optical properties in small volumes of turbid media," Appl. Opt. **46**(29), 7317–7328 (2007).
18. A. Kim, M. Roy, F. Dadani, and B. C. Wilson, "A fiberoptic reflectance probe with multiple source-collector separations to increase the dynamic range of derived tissue optical absorption and scattering coefficients," Opt. Express **18**(6), 5580–5594 (2010).
19. V. Krishnaswamy, A. M. Laughney, K. D. Paulsen, and B. W. Pogue, "Dark-field scanning *in situ* spectroscopy platform for broadband imaging of resected tissue," Opt. Lett. **36**(10), 1911–1913 (2011).
20. P. D. Ninni, F. Martelli, and G. Zaccanti, "Intralipid: towards a diffusive reference standard for optical tissue phantoms," Phys. Med. Biol. **56**(2), N21–N28 (2011).
21. H. J. van Staveren, C. J. Moes, J. van Marle, S. A. Prahl, and M. J. van Gemert, "Light scattering in Intralipid-10% in the wavelength range of 400-1100 nm," Appl. Opt. **30**(31), 4507–4514 (1991).
22. G. Zaccanti, S. Del Bianco, and F. Martelli, "Measurements of optical properties of high-density media," Appl. Opt. **42**(19), 4023–4030 (2003).
23. F. Martelli and G. Zaccanti, "Calibration of scattering and absorption properties of a liquid diffusive medium at NIR wavelengths. CW method," Opt. Express **15**(2), 486–500 (2007).
24. R. Michels, F. Foschum, and A. Kienle, "Optical properties of fat emulsions," Opt. Express **16**(8), 5907–5925 (2008).
25. T. J. Farrell, M. S. Patterson, and B. Wilson, "A diffusion theory model of spatially resolved, steady-state diffuse reflectance for the noninvasive determination of tissue optical properties *in vivo*," Med. Phys. **19**(4), 879–888 (1992).
26. S. L. Jacques and B. W. Pogue, "Tutorial on diffuse light transport," J. Biomed. Opt. **13**(4), 041302 (2008).
27. J. R. Mourant, J. Boyer, A. H. Hielscher, and I. J. Bigio, "Influence of the scattering phase function on light transport measurements in turbid media performed with small source-detector separations," Opt. Lett. **21**(7), 546–548 (1996).
28. F. Bevilacqua and C. Depeursinge, "Monte Carlo study of diffuse reflectance at source–detector separations close to one transport mean free path," J. Opt. Soc. Am. A **16**(12), 2935–2945 (1999).
29. A. Kienle, F. K. Forster, and R. Hibst, "Influence of the phase function on determination of the optical properties of biological tissue by spatially resolved reflectance," Opt. Lett. **26**(20), 1571–1573 (2001).
30. I. S. Saidi, S. L. Jacques, and F. K. Tittel, "Mie and Rayleigh modeling of visible-light scattering in neonatal skin," Appl. Opt. **34**(31), 7410–7418 (1995).
31. P. R. Bargo, S. A. Prahl, T. T. Goodell, R. A. Sleven, G. Koval, G. Blair, and S. L. Jacques, "*In vivo* determination of optical properties of normal and tumor tissue with white light reflectance and an empirical light transport model during endoscopy," J. Biomed. Opt. **10**(3), 034018 (2005).
32. E. L. Hull and T. H. Foster, "Steady-state reflectance spectroscopy in the P3 approximation," J. Opt. Soc. Am. A **18**(3), 584–599 (2001).
33. F. Bevilacqua, D. Piguet, P. Marquet, J. D. Gross, B. J. Tromberg, and C. Depeursinge, "*In vivo* local determination of tissue optical properties: applications to human brain," Appl. Opt. **38**(22), 4939–4950 (1999).
34. S. C. Kanick, U. A. Gamm, H. J. C. M. Sterenborg, D. J. Robinson, and A. Amelink, "Method to quantitatively estimate wavelength-dependent scattering properties from multidiameter single fiber reflectance spectra measured in a turbid medium," Opt. Lett. **36**(15), 2997–2999 (2011).
35. S. C. Kanick, U. A. Gamm, M. Schouten, H. J. C. M. Sterenborg, D. J. Robinson, and A. Amelink, "Measurement of the reduced scattering coefficient of turbid media using single fiber reflectance spectroscopy: fiber diameter and phase function dependence," Biomed. Opt. Express **2**(6), 1687–1702 (2011).
36. S. C. Kanick, H. J. C. M. Sterenborg, and A. Amelink, "Empirical model of the photon path length for a single fiber reflectance spectroscopy device," Opt. Express **17**(2), 860–871 (2009).
37. W. F. Cheong, S. A. Prahl, and A. J. Welch, "A review of the optical properties of biological tissues," IEEE J. Quantum Electron. **26**(12), 2166–2185 (1990).
38. L. Wang, S. L. Jacques, and L. Zheng, "MCML--Monte Carlo modeling of light transport in multi-layered tissues," Comput. Methods Programs Biomed. **47**(2), 131–146 (1995).
39. S. C. Kanick, D. J. Robinson, H. J. C. M. Sterenborg, and A. Amelink, "Monte Carlo analysis of single fiber reflectance spectroscopy: photon path length and sampling depth," Phys. Med. Biol. **54**(22), 6991–7008 (2009).

40. B. W. Pogue and G. Burke, "Fiber-optic bundle design for quantitative fluorescence measurement from tissue," Appl. Opt. **37**(31), 7429–7436 (1998).
41. U. A. Gamm, S. C. Kanick, H. J. C. M. Sterenborg, D. J. Robinson, and A. Amelink, "Measurement of tissue scattering properties using multi-diameter single fiber reflectance spectroscopy: *in silico* sensitivity analysis," Biomed. Opt. Express **2**(11), 3150–3166 (2011).
42. B. Gélébart, E. Tinet, J. Tualle, and S. Avrillier, "Phase function simulation in tissue phantoms: a fractal approach," Pure Appl. Opt. **5**(4), 377–388 (1996).
43. J. Pyhtila, R. Graf, and A. Wax, "Determining nuclear morphology using an improved angle-resolved low coherence interferometry system," Opt. Express **11**(25), 3473–3484 (2003).
44. Y. L. Kim, Y. Liu, R. K. Wali, H. K. Roy, M. J. Goldberg, A. K. Kromin, K. Chen, and V. Backman, "Simultaneous measurement of angular and spectral properties of light scattering for characterization of tissue microarchitecture and its alteration in early precancer," IEEE J. Sel. Top. Quantum Electron. **9**(2), 243–256 (2003).

1. Introduction

Reflectance spectroscopy provides estimates of optical properties within a turbid medium such as tissue. This modality has an important role in the field of biomedical optics, as reflectance spectra can be used to extract information about aspects of the tissue physiology (*e.g.* vascular oxygen saturation and blood volume fraction) [1,2] and morphology (*e.g.* cell, organelle size and density) [3–6] and can be used to correct raw fluorescence measurements for the influences of background scattering and absorption [7–9]. Spectra measured in reference media such as the fat emulsion commercialized as Intralipid (IL) are often used to calibrate or understand instrument performance [10], yet the spectra recorded by different devices can be dramatically affected by device-specific sensitivities to the scattering properties. In this study, the influence of detection geometry with respect to IL concentration is studied in detail using measurements and Monte Carlo studies, to illustrate and interpret how the spectra can change.

Fiber optic reflectance devices are designed to sample light from a location of interest where typically the size and shape is customized for the biological application. Devices that collect reflectance remitted at large distances from the source can achieve (relatively) deep sampling and therefore are capable of monitoring volume averaged quantities in bulk tissues such as blood oxygenation in the brain [11] or breast [12]. Conversely, devices that collect reflectance close to the light source sample highly localized volumes, and therefore can provide selective sampling of superficial tissue layers [13–19]. Validation of these devices with tissue-simulating optical phantoms *in vitro* is critical to allow characterization of the observed reflectance in response to controlled optical properties within the phantom. Phantom measurements may also be a valuable method to calibrate the wavelength-specific device response for use in analyzing measurements of media with unknown optical properties, such as tissue. Perhaps the most commonly adopted scattering phantom is IL [10,20], because it is stable across batches, readily purchased and has been extensively investigated to characterize the wavelength-dependent optical properties [21–24]. Dilutions of IL can yield wavelength-dependent reduced scattering coefficients (μ_s') that are similar to values reported in tissue. These characteristics have led to wide acceptance of IL as a tissue-simulating scattering standard for the investigation of many types of reflectance devices [13,15–19]. However, as this study shows, spectra measured in the same IL phantom by different reflectance geometries may show substantially different spectral features.

To understand how scattering properties influence reflectance spectra measured by different device geometries differently, it is important to consider the influence of scattering on the transport of light being collected during measurements. Light that travels relatively large distances in scattering media is termed diffuse, with photon transport occurring in the direction of fluence (concentration) gradients within the medium [25,26]. Collected diffuse reflectance intensities can be described analytically by the diffusion approximation to the radiative transport equation, which allows estimation of both μ_s' and the absorption coefficient (μ_a) [18,25]. The heuristic guideline for diffuse transport is light that has
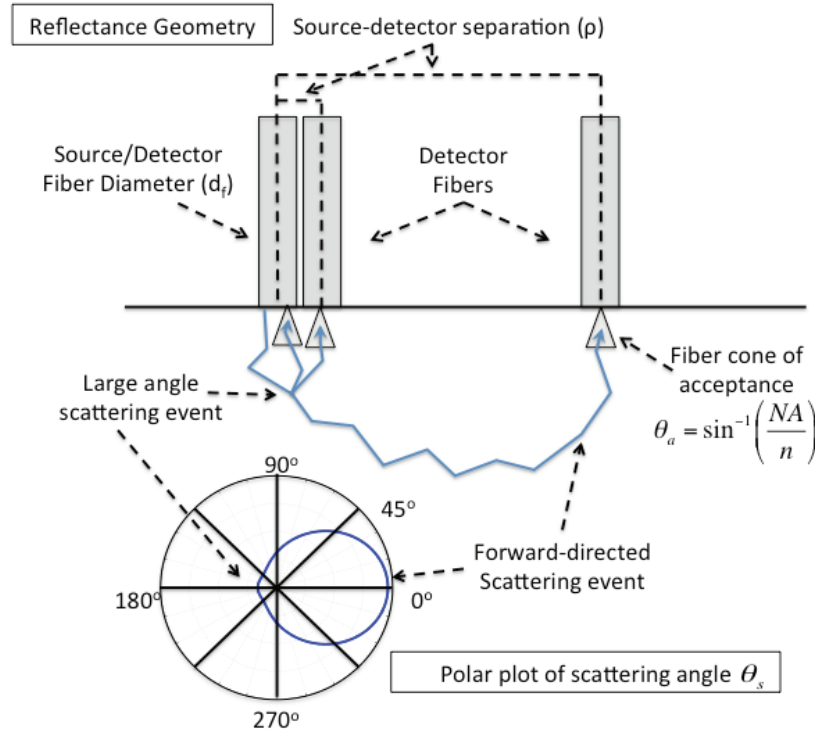
Fig. 1. Fiber optic geometries of reflectance devices that measure light close to the source fiber. Single fiber measurements obtained using same fiber optic to deliver and collect light with diameter given by d_f. Separate source detector devices have core-to-core separations given by rho. Light transport from source to detectors show geometry-specific dependence on the probability of scattering events specified by the scattering phase function. Polar plot shows phase function for Intralipid at 400 nm.

travelled 1 to 2 mean free transport lengths from the source [26]; here, the term transport length is defined as $(\mu_s' + \mu_a)^{-1}$. Analysis of diffuse light is insensitive to the form of the scattering phase function (PF), as changes to the scatter frequency (given by μ_s) and directionality (given by PF) interchangeably influence diffuse light transport in the form of the reduced scattering coefficient $\mu_s' = \mu_s(1-g)$, where g is the anisotropy given as $g = \langle \cos\Theta_s \rangle$. As the distance between source and collection location decreases, the sampled transport regime shifts from the collection of multiply scattered light to the collection of photons that may have undergone few (or single) scattering events [27,28]. Light transport in this semi- to non-diffuse regime is not exclusively characterized by μ_s', but is also influenced by the probability of large angle backscattering events, which is defined by the scattering PF [28,29].

The influence of PF on light transport collected at various source-detector separations (ρ) is illustrated in Fig. 1. Light collected at large ρ is multiply scattered, making it insensitive to any individual directional scattering event. Light collected at small ρ is sensitive to large angle scattering events. The frequency of these events is proportional to the magnitude of the backscatter-lobe of the PF. In IL phantoms, it is important to consider that both μ_s' and PF change considerably over the ultraviolet-visible (UV-vis) wavelength range; these changes are displayed in Fig. 2 (A) and (B), respectively. While it is well known that μ_s' exhibits a power law relationship with wavelength [30,31], changes to PF vs. wavelength are less commonly understood. In Fig. 2 (B), PFs from selected wavelengths are plotted as the probability density distributions of scattering angles; these plots show marked differences between wavelengths
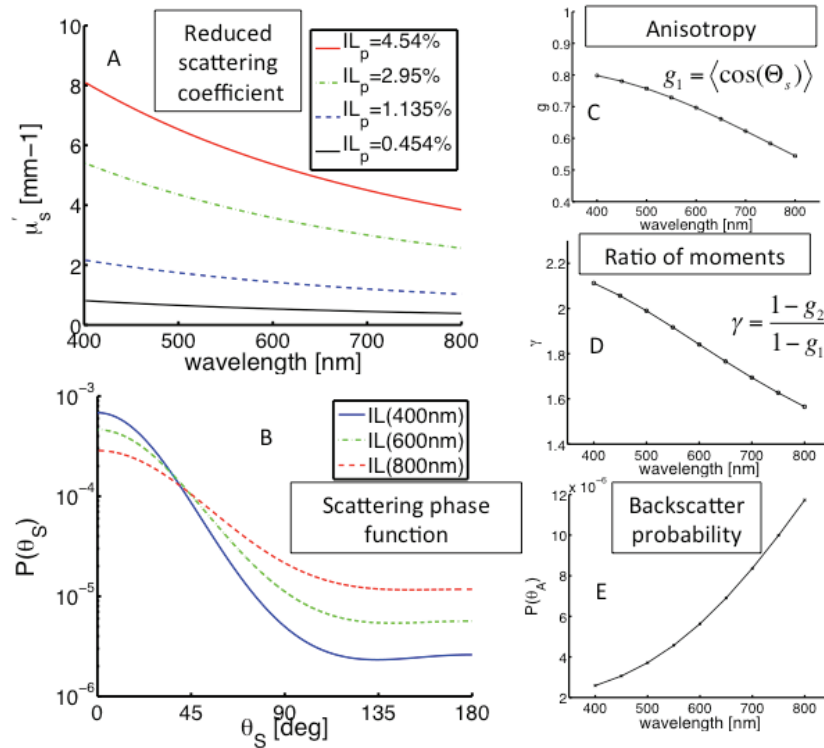
Fig. 2. Optical properties of Intralipid optical phantoms. A) shows reduced scattering coefficient vs. wavelength for selected IL dilutions. B) scattering phase function of IL at selected wavelengths. Right column shows wavelength-dependent metrics of PF: C) anisotropy, D) ratio of the first and second moments of the phase function, and the E) probability of large angle backscatter events. This study assumes that reduced scattering coefficient linearly relates to dilutions of IL, while PF-related parameters are dilution independent.

[24]. Previous studies have developed metrics to describe the average directional scattering behavior associated with a PF [28,32]. Specifically, these studies utilized Legendre moments of the PF distributions to characterize the average direction of scatter, given by the anisotropy ($g = g_1$), which is shown in Fig. 2 (C), and the likelihood of large angle backscatter events, given by a parameter $\gamma = \dfrac{1-g_2}{1-g_1}$ which includes information about the first two moments of the PF, g_1 and g_2, respectively and is shown in Fig. 2 (D). For forward-directed scattering media, such as IL, γ can be interpreted as follows: decreases in values of γ are associated with an increased likelihood of large angle backscatter events. A simple approach to characterizing the differences in the likelihood of backscatter between PFs is to consider the probability of a large angle backscatter event, which we define as an scattering angle that would fall within the cone of acceptance for the fiber probes included in this study. Consideration of these large angle events is especially relevant for the single scattering regime. Figure 2 (E) shows that for IL, the likelihood of large angle backscattering events increases substantially across the UV-vis wavelength range; correspondingly, γ decreases over the same range. Previous studies have utilized the moments of the PF to describe collected light intensity near the source [28,32–34]. But to the best of the author's knowledge, these findings have not been translated to the characterization of scattering-induced spectral features for devices that measure over different length scales close to the source, even for a well-characterized scattering standard such as IL.

This study characterizes scattering features observed in reflectance spectra measured in IL optical phantoms. Experimental and simulation data are used to identify and investigate the spectral response of reflectance measured in a wide range of IL dilutions as measured by fiber optic device geometries with 1) overlapping source and detector with a range of fiber diameters, and 2) separate source and detector fibers with a wide range of source-detector separations. The underlying mechanisms that link the observed spectral response to the wavelength-dependent scattering properties are presented, and the potential errors associated with a failure to consider PF-related effects for measurements close to the source are discussed.

2. Methods

2.1. Single fiber reflectance experimental setup

The experimental apparatus for the reflectance device that uses a single fiber optic to deliver and collect light during measurements has been described in detail previously [35,36]. The device consists of a halogen light source (HL-2000-FHSA, Ocean Optics, Duiven, Netherlands), a spectrometer (SD2000, Ocean Optics, Duiven, Netherlands) and a solid core single fiber probe that is connected to the light source and the spectrometer via a bifurcated fiber. The probe tip is polished at an angle of 15 degrees to remove specular reflections within the collected reflectance intensity due to the index of refraction mismatch at the probe/medium interface. This study used a calibration procedure to account for variations in the output of the lamp, transmission characteristics of the fiber, and sensitivity of the spectrometer. Calibration measurements were performed in a calibration phantom containing 20% IL diluted to a volume particle concentration of 1.5%, which yielded μ_s' (800 nm) = 1.2 mm^{-1} ($I_{IL}^{cal}(\lambda)$), and in a dark container filled with water ($I_{water}(\lambda)$):

$$R_{SF}^o(\lambda) = I_{IL}^{sim}(\lambda)\left(\frac{I_{phantom}(\lambda) - I_{water}(\lambda)}{I_{IL}^{cal}(\lambda) - I_{water}(\lambda)}\right) \tag{1}$$

Here, $I_{phantom}(\lambda)$ is the raw signal of a sampled optical phantom, and $I_{IL}^{sim}(\lambda)$ is the absolute single fiber reflectance (SFR) signal, expressed in % of incident photons, obtained by Monte Carlo (MC) simulations of the IL calibration phantom. Importantly, for these simulations the wavelength-specific PFs and μ_s' values reported by [24] were used. The calculation results in the calibrated single fiber reflectance intensity, $R_{SF}^o(\lambda)$.

2.2. Intralipid tissue simulating phantom preparation

The liquid phantoms were prepared by mixing 0.9% NaCl (Baxter, Utrecht, Netherlands) with different amounts of Intralipid 20% (Fresenius Kabi, s-Hertogenbosch, Netherlands); this stock solution has a volume particle concentration percentage (IL$_p$) of 22.7% [22]. Phantoms were prepared in volumes of 20 ml with dilutions resulting in IL$_p$ values of [0.455, 0.568, 0.908, 1.135, 1.476, 2.951, 4.540] %. The reduced scattering coefficient of the Intralipid stock solution was determined to be μ_s' (800 nm) = 18.6 mm^{-1} by using the formula given by Michels et al. [24]. The dependence of μ_s' on the Intralipid concentration was assumed to be linear (for the range of concentrations investigated) and the resulting wavelength-dependent μ_s' is given for selected phantoms in Fig. 2 (A). The dilutions selected for this study resulted in a range of $\mu_s' = $ [0.4-8] mm^{-1} that is representative of the values reported in tissue [37].

Reflectance measurements were performed by submerging the probe tip a few millimeters into the phantom and suspending it multiple centimeters from the container bottom or sides, such that the probe would not collect reflections from container surfaces. The measurement

was repeated 3 times for each phantom, with these spectra averaged for each phantom. All measurements were performed with 5 fiber probes of diameter: [0.2, 0.4, 0.6, 0.8, 1.0] mm. The phantom was gently agitated before collecting each spectrum to ensure homogeneity. Measurements were reproducible, with variation between repeated measurements of < 3%.

2.3. Monte Carlo simulations of reflectance measurements

The Monte Carlo code utilized in this study is based on the steady state light transport in multi-layered structures (MCML) approach to stochastically simulate photon propagation within a turbid medium [35,38,39]. The code was adapted to simulate the measurement of reflectance intensity from a turbid medium with homogeneously distributed optical properties; this model of photon propagation has previously been described in detail and will be reviewed here briefly. Photons were initialized by selecting a location on the fiber face in contact with the medium and were launched into a direction within the fiber cone of acceptance, given as $\theta_a = sin^{-1}\left(\dfrac{NA}{n}\right)$, with the fiber numerical aperture (NA) and the index of refraction of the medium given by n. Both location and direction were sampled from uniform distributions. The fiber probes were modeled in contact with the turbid medium at an air interface, with n of the medium set to 1.33 and that of the fiber to 1.45. The fiber NA was specified as 0.22. Reflection and refraction at the boundary between fiber face and medium were accounted for by using Fresnel's equation and Snell's law. The photons were propagated through the medium in discrete steps selected from an exponential distribution that was weighted by the scattering coefficient. Each scattering event resulted in a change in propagation direction that was sampled from a discrete user-specified PF distribution. Photons that contacted the detector fiber within the cone of acceptance were collected. For all simulations, photons that propagated far from the fiber face did not contribute to the collected reflectance intensity and were terminated at a hemispherical limit from the source fiber at a distance great enough to not influence the model outputs for the range of optical properties investigated in this study. The collection area for the single fiber simulations overlapped the source fiber location, with d_f specified in the range [0.2, 0.4, 0.6, 0.8, 1.0] mm. For separate source detector devices, source and detector fiber diameters were fixed to 0.2 mm, and photons were collected using annular areas at appropriate radial distance such that the core-to-core separation ρ was specified in the range [0.2, 0.4, 0.6, 1.0, 2.0] mm. Simulations returned collected reflectance intensity in the absence of absorption, and also returned the weighted average number of scattering events experienced by collected photons from each measurement. Reflectance intensity returned for separate source detector simulations was calculated by the ratio of the total number of photons collected (TPC) by the total number of photons launched (TPL) and corrected for differences in collection area (A), as

$$R_{SD}^N(\lambda) = \left(\frac{1}{A}\right)\left(\frac{TPC}{TPL}\right) \tag{2}$$

The optical properties of the simulated medium were selected to mimic IL phantoms. The reduced scattering coefficient was specified by linearly scaling the μ_s' of the IL 20% stock solution, given in [24] for the selected IL dilutions. Simulations of single fiber reflectance probes were performed to match the measured optical phantoms, and simulations for the separate source detector device were performed for IL dilutions resulting in IL_p values of [0.454, 0.568, 1.135, 2.270, 3.405, 4.540, 5.675]. Wavelength-dependent PFs were specified using empirical formulas also reported in [24], with simulations performed at discrete wavelengths between 400 and 800 nm at 100 nm increments. Each simulation initialized between 10 and 100 million photons.

3. Results

3.1. Reflectance measurement of IL phantoms with a single fiber device

Figure 3 shows a comparison of reflectance spectra measured in IL optical phantoms by reflectance devices that use a single fiber optic to deliver and collect light. Panels (A), (B) and (C) contain spectra measured in a dilution series of IL phantoms, with IL_p in the range [0.454–4.54]%, with each panel showing spectra obtained by a different fiber diameter from the series [0.2, 0.4, 1.0] mm. Initial inspection of the data show expected trends of increased $R_{SF}^o(\lambda)$ in response to increases in IL_p, which is observed by comparison of spectra within each panel. $R_{SF}^o(\lambda)$ also increases with increases in d_f, which is observed by comparison of spectra between different panels. A closer inspection of the spectra shows that the wavelength-dependent spectral shape of each curve changes with respect to changes in IL_p and d_f. Figure 3 (D) and (E) show normalized $R_{SF}^o(\lambda)$ spectra measured by 3 different fiber diameters in selected IL_p phantoms of 4.54% and 0.454%, respectively. Spectra are normalized to the intensity at 400 nm to highlight the substantial differences in spectral shapes returned by measurements with different fiber diameters. First we consider the spectra measured by d_f =
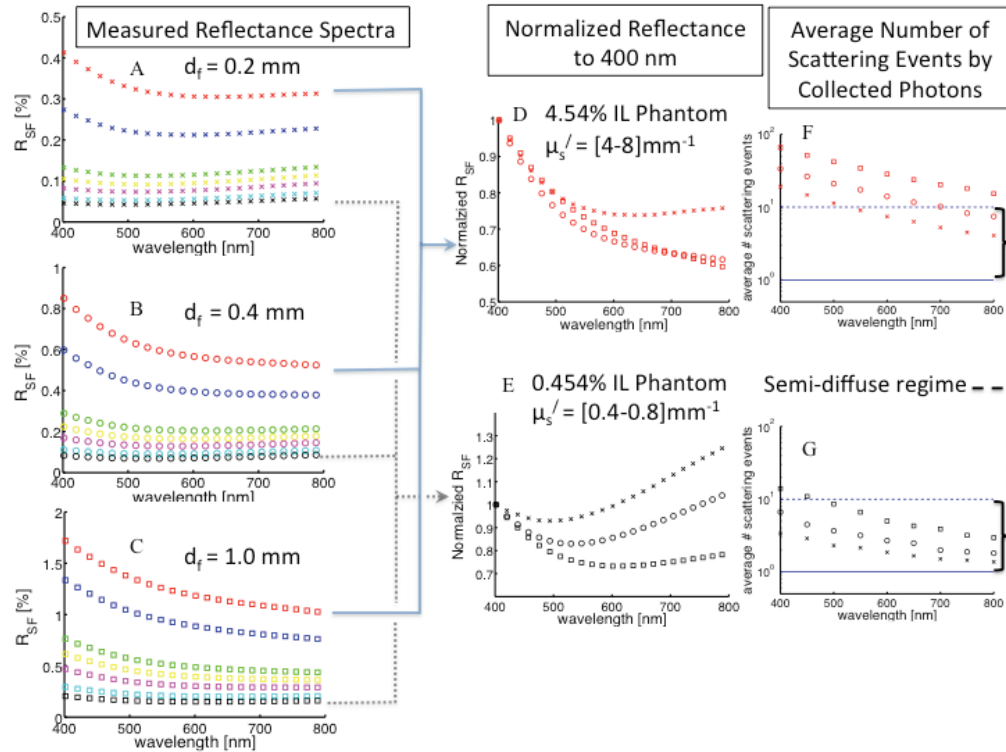

Fig. 3. Analysis of spectral scattering features observed in experimentally measured reflectance collected by single fiber reflectance device. Left hand column presents calibrated reflectance spectra as measured with single fiber diameters of A) 0.2 (x marks), B) 0.4 (circle marks), and C) 1.0 mm (square marks). Each panel shows spectra measured from dilutions of IL resulting in volume particle concentrations of [0.455, 0.568, 0.908, 1.135, 1.476, 2.951, 4.540]% that are indicated by colors [red, blue, green, yellow, magenta, cyan, and black], respectively. Middle column shows selected spectra measured by each fiber in D) 4.54% and E) 0.454%, with each spectra normalized at 400 nm for comparative purposes. Right hand column shows the average number of scattering events experienced by photons at discrete wavelengths for spectra in F) 4.54% and G) 0.454% phantoms.

1 mm in the $IL_p = 4.54\%$ phantom, where $R_{SF}^o(\lambda)$ monotonically decreases vs. wavelength. Reflectance spectra measured by smaller fibers in the same phantom show a transition to a more complicated biphasic behavior. Specifically for $d_f = 0.2$ mm, $R_{SF}^o(\lambda)$ monotonically decreases over 400-500 nm, but exhibits a plateauing effect over 500-800 nm. For the lower scattering phantom, with $IL_p = 0.454\%$, reflectance spectra exhibit the biphasic behavior for $d_f = [0.2, 0.4, 1.0]$ mm, with $R_{SF}^o(\lambda)$ decreasing over 400-500 nm followed by $R_{SF}^o(\lambda)$ increasing from 500 to 800 nm. The data in panels (D) and (E) show that the wavelength-dependent changes in R_{SF}^o measured in the same phantom are substantially different between different fiber diameters. For example, reflectance spectra measured in the 4.54% phantom show a decrease in R_{SF}^o from 400 to 800 nm of 25% for $d_f = 0.2$ mm, and 45% for $d_f = 1.0$ mm. Moreover, the R_{SF}^o data show substantially different spectral responses for measurements of phantoms with different IL dilutions with the same fiber diameter. For example, reflectance spectra measured with a fiber with $d_f = 0.4$ mm in the 4.54 and 0.454% IL_p phantoms show of decrease of 40% and an increase of 5%, respectively.

Understanding the mechanisms underlying these spectral differences requires consideration of two contributing factors: 1) how scattering influences light propagation during measurement and, 2) how these influences change over the wavelength range sampled in the IL phantoms. It is understood that reflectance devices sample photons that have experienced a range of scattering events [27]. For reflectance measured near the source, decreases in μ_s' or d_f are likely to decrease the number of scattering events experienced by collected photons [40], which in turn increases the sensitivity of the collected reflectance intensity to PF-effects. In IL the scattering properties that influence light transport (μ_s' and PF) change substantially across the UV-vis wavelength range. Figure 2 (A) shows $\mu_s'(\lambda)$ over 400-800 nm. The PF also changes over the same wavelength range, with $\gamma(\lambda)$ showing that the likelihood of backscatter events increases vs. wavelength. To characterize the link between these wavelength-dependent optical properties and the observed reflectance, we considered the scattering histories of photons collected across the sampled wavelength range. For this purpose, a Monte Carlo model was used to return the average number of scattering events for photons collected at discrete wavelengths along each spectrum reported Fig. 3 (D) and (E); the corresponding scattering event data are shown in panels (F) and (G), respectively. These scattering data are plotted on a log-scale and include annotations to highlight two important thresholds: 1) the single scattering baseline, and 2) an approximate limit to the diffuse regime of 10 scattering events. We first consider the reflectance spectrum that exhibited single-phase behavior, ($d_f = 1$ mm measurement of the 4.54% IL_p phantom). Light collected across this spectrum was, on average, multiply scattered (with >10). The resulting diffuse signal is expected to be insensitive to PF-effects, a claim that is supported by agreement in wavelength-dependent trends of $R_{SF}^o(\lambda)$ and $\mu_s'(\lambda)$ over the sampled wavelength range. Inspection of scattering data for reflectance curves that exhibit the convex biphasic behavior shows that the collected photons often experienced few (<10) scattering events. These measurements contained contributions from photons sampled in the semi-diffuse regime and are expected to be sensitive to the wavelength-dependent changes in PF. This claim is supported by considering that the observed increase in $R_{SF}^o(\lambda)$ vs. wavelength in the 500–800 nm region for these spectra is correlated with the wavelength-dependent changes in backscatter probability described by $\gamma(\lambda)$ and PF(θ_a) as observed in Fig. 2. These data indicate that the spectral features observed in $R_{SF}^o(\lambda)$ spectra measured in IL phantoms are attributable to the sensitivity of the reflectance device to the combined wavelength

dependent changes in $\mu_s'(\lambda)$ and PF in IL. While the combined influence of μ_s' and PF on R_{SF}^o at a single wavelength has been modeled in detail previously [34,41]; these data present a qualitative representation of how wavelength-dependent features in reflectance spectra are affected by the wavelength dependent scattering properties and device geometry.

The spectral features observed in single fiber reflectance spectra measured in IL phantoms highlight the changing influence of PF across the wavelengths of a single spectrum; these changes can have profound effects on the relationship between R_{SF}^o and μ_s'. The left column of Fig. 4 shows R_{SF}^o vs. μ_s' measured in all IL phantoms with panels (A), (B), and (C), showing measurements by d_f = [0.2, 0.4, 1.0] mm, respectively. Here, colors are used to indicate wavelength. These data show that R_{SF}^o cannot be used to uniquely identify μ_s', because PF-effects influence the proportionality between $R_{SF}^o(\lambda)$ and μ_s' differently at each wavelength. This statement is evidenced by the data in Figs. 3 (D) and 3(E), where $R_{SF}^o(\lambda)$ does not explicitly follow $\mu_s'(\lambda)$, but is also influenced by $\gamma(\lambda)$. Comparison of measurements from different fiber diameters showed an underlying relationship between R_{SF}^o and the dimensionless reduced scattering coefficient, given as $\mu_s'd_f$. Figure 4 panel (D) contains measurements from all investigated fiber diameters, d_f [0.2, 0.4, 0.6, 0.8, 1.0] mm,
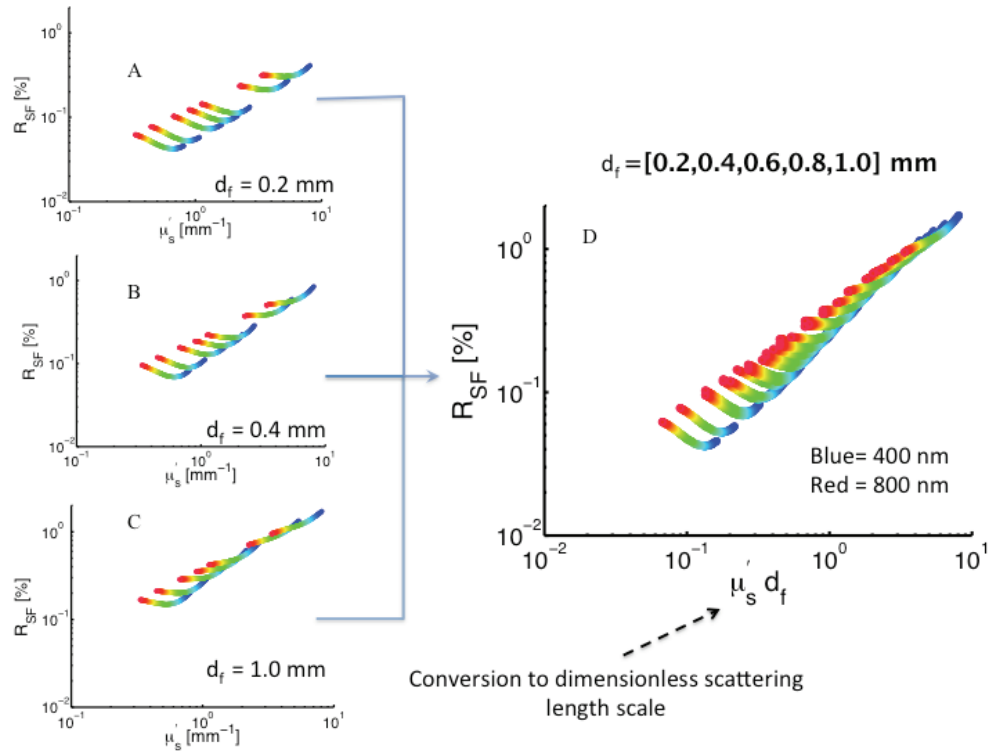

Fig. 4. Relationship between experimentally measured single fiber reflectance intensity and scattering properties in IL phantoms. Left hand column shows reflectance intensities vs. reduced scattering coefficient for fiber diameters of A) 0.2, B) 0.4, and C) 1.0 mm. Panel D) shows reflectance intensities vs. dimensionless reduced scattering for all measured fibers. In this plot color indicates different wavelengths and can be used to interpret the phase function specific proportionalities between reflectance intensity and reduced scattering coefficient, with colors transitioning from blue (at 400 nm) to red (at 800 nm).

in investigated phantoms with IL_p in the range of [0.454–4.54]%. Inspection of the R_{SF}^o data show that for increasing $\mu_s' d_f$ values, less stratification is observed between different wavelengths, meaning that the collected intensities are less influenced by PF. This is consistent with previous work that identified a threshold limit of PF-independent behavior for values of $\mu_s' d_f > 10$ [35]. This plot shows that reflectance intensity collected by a single fiber optic is interchangeably influenced by μ_s' and d_f and highlights the influence of the wavelength-dependent PF on R_{SF}^o.
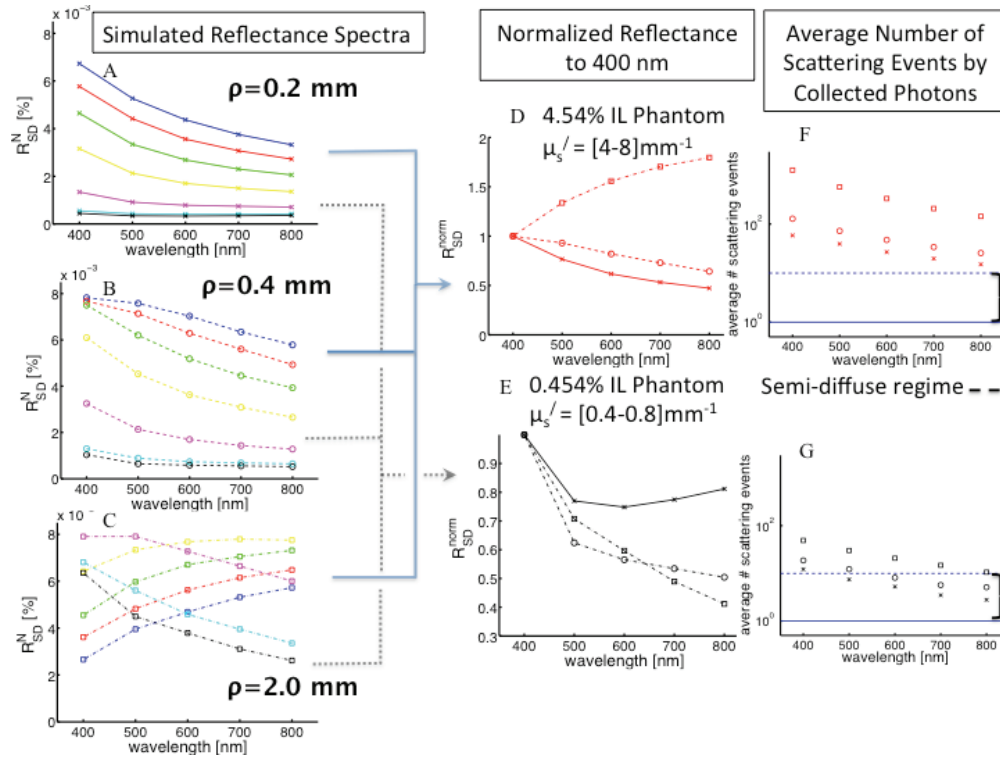

Fig. 5. Analysis of spectral scattering features observed in simulated reflectance spectra collected by devices with separate source and detector. Left hand column shows dimensionless reflectance spectra returned using selected source detector separations of A) 0.2 (x marks), B) 0.4 (circle marks), and C) 1.0 mm (square marks). Each panel shows spectra simulated from dilutions of IL resulting in volume particle concentrations of [0.455, 0.568, 0.908, 1.135, 1.476, 2.951, 4.540]% that are indicated by colors [blue, red, green, yellow, magenta, cyan, and black], respectively. Middle column shows spectra returned by 3 selected source-detector separations in D) 4.54% and E) 0.454% phantoms, with the spectra normalized at 400 nm for comparative purposes. Right hand column shows the average number of scattering events experienced by photons at discrete wavelengths for spectra in F) 4.54% and G) 0.454% phantoms.

3.2. Reflectance measurement of IL phantoms with separate source-detector fibers

Figure 5 shows simulated reflectance measurements in IL optical phantoms performed with separate source and detector fibers. Here, panels (A), (B), and (C) contain spectra measured in a dilution series of IL phantoms, in the range [0.454–5.675]%, with each panel showing data obtained by a source-detector separation from the series $\rho = [0.2, 0.4, 2.0]$ mm. Initial inspection of these data show a complicated dependence of $R_{SD}^N(\lambda)$ on the phantom IL_p. For adjacent source-detector fibers ($\rho = 0.2$ mm), an increase in IL_p results in an increased

reflectance intensity across the entire spectrum. This is not the case for source detectors with large separation (ρ = 2.0 mm), as increases in IL_p from 0.4 to 1.0% result in increased R_{SD}^N, but increases in IL_p from 2 to 5% result in decreased R_{SD}^N; this nonlinear dependence of R_{SD}^N on μ_s' is described by diffusion theory and has been characterized in detail previously [18]. In order to understand the influence of scattering properties on the spectral response, we first compare spectra measured in the same phantom with different ρ. Figure 5 panels (D) and (E) show reflectance spectra measured at 3 different source detector separations in phantoms with IL_p of 4.54% and 0.454%. The panels (F) and (G) show the average number of scattering events corresponding to discrete wavelengths in the spectra plotted on panels (D) and (E), respectively. The normalized spectra from the 4.54% IL_p phantom show decreases in $R_{SD}^N(\lambda)$ vs. wavelength for the small fiber separations (ρ = [0.2, 0.4] mm), but an increase of $R_{SD}^N(\lambda)$ vs. wavelength for the large ρ (2.0 mm). The latter spectrum can be described by increases in μ_s' vs. wavelength increasingly attenuating the collected reflectance intensity; therefore $R_{SD}^N(\lambda)$ follows the inverse trend of $\mu_s'(\lambda)$ vs. wavelength over the sampled wavelength range. Inspection of the scattering data for these spectra in panel (F) show that these measurements sample diffuse light, and are independent of PF. Figure 5 panel (E) shows normalized reflectance spectra measured in the 0.454% IL_p phantom at different ρ. These data show a transition from $R_{SD}^N(\lambda)$ monotonically decreasing vs. wavelength (for ρ = 2.0 mm) to biphasic behavior (for ρ = 0.2). Inspection of the number of scattering events experienced by collected photons in panel (G), shows a transition from sampling multiply scattered light in the diffuse regime (for ρ = 2.0 mm) to the sampling of fewer scattering events in the semi-diffuse regime (for ρ = 0.2 mm). These observations are consistent with the concept that measurements close to the source are more likely to be sensitive to the frequency of large angle backscatter events, and therefore the collected spectrum is influenced by PF-effects.

Figure 6 shows analysis of the relationship between R_{SD}^N and μ_s' for separate source detector devices. Panels (A), (B), and (C) show R_{SD}^N vs. μ_s' for measurements of phantoms with a wide range of IL_p, with each panel showing measurements from a device with ρ = [0.2, 0.4, 2.0] mm. R_{SD}^N measurements close to the source (ρ = 0.2 and 0.4 mm) show a sensitivity to PF effects for small μ_s' values; this is characterized by the non-unique relationship between R_{SD}^N and μ_s' in the low scattering region. For ρ = 0.2 and 0.4 mm devices, as μ_s' increases the R_{SD}^N shows less stratification due to PF-effects and the data transition to PF-insensitivity for large μ_s' values; this transition follows the shift from sampling predominantly in the semi-diffuse regime to the diffuse regime as scattering increases. The data for the large source detector separation of ρ = 2.0 mm shows a distinct nonlinear dependence on μ_s', with the R_{SD}^N vs. μ_s' showing a monotonically increasing region that transitions through a peak into a monotonically decreasing region; this transition occurs for measurements sampling diffuse light that are independent of PF effects. Inspection of the reflectance data measured at different ρ shows an underlying relationship that is identified by conversion of the x-axis to the dimensionless reduced scattering coefficient, here given as $\mu_s'\rho$, and conversion of the y-axis to $R_{SD}^N\rho^2$. Figure 6 panel (D) contains measurements from all investigated source-detector separations ρ = [0.2, 0.4, 0.6, 1.0, 2.0] mm in all simulated IL phantoms IL_p = [0.454-5.675] %. These data show that $R_{SD}^N\rho^2$ is influenced similarly by $\mu_s'\rho$ for different ρ.

Inspection of these data showed that for $\mu_s'\rho > 0.5$, R_{SD}^N showed less than 10% variation about the mean value, and are therefore considered independent of PF influences at different
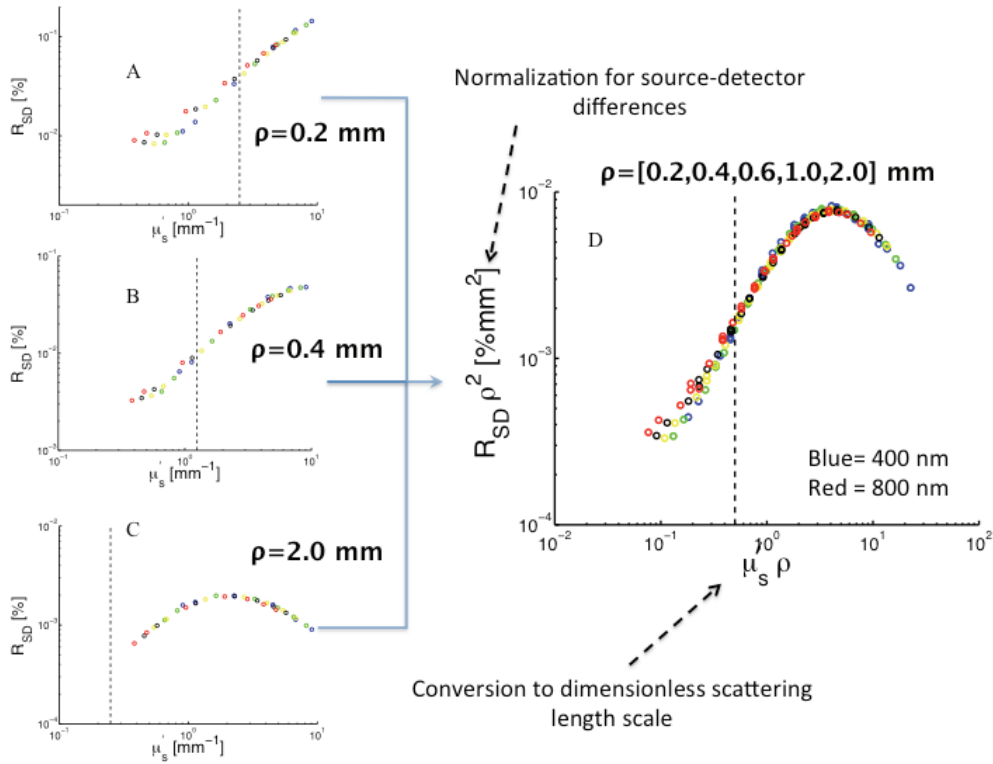
Fig. 6. Relationship between reflectance intensity returned by simulations of separate source-detector geometries and scattering properties in IL phantoms. Left hand column shows reflectance intensities vs. reduced scattering coefficient for source-detector separations of A) 0.2, B) 0.4, and C) 2.0 mm. Panel D) shows reflectance intensities vs. dimensionless reduced scattering for all measured separations. In this plot color indicates different wavelengths with [400, 500, 600, 700, 800] nm indicated by [blue, green yellow, black, red], respectively. Vertical dashed lines indicate the empirically identified threshold for observed PF-sensitivity of the reflectance at small dimensionless scattering values.

wavelengths. This threshold was used to identify the smallest μ_s' that could be sampled independent of PF for each ρ. For separate source detectors of ρ = [0.2, 0.4, 2.0] mm, the lower bound of μ_s' was estimated as [2.5, 1.25, 0.25] mm^{-1}, respectively. These thresholds are included as vertical dashed lines on plots in Fig. 6 to allow visualization of scattering regions influenced by PF and independent of PF.

4. Discussion

IL optical phantoms have substantial wavelength-dependent changes in μ_s' and PF in the UV-vis region. This study characterizes how these scattering properties influence spectral features of reflectance measured close to the source. Experiments and simulations were used to investigate reflectance spectra returned in a set of IL phantoms that contained a wide range of μ_s' values. Reflectance spectra were measured or simulated for device geometries that delivered and collected with either a single fiber or separate fibers. Data show that changes to the observed spectral remission characteristics occur in response to slight changes in either measurement geometry or IL dilution. These changes are related to the light transport regime sampled, with spectral features showing a (non-linear) dependence on μ_s' for measurements that collect diffusely scattered light, and on top of that a dependence on PF for measurements that collect semi-diffuse light.

Tissue simulating optical phantoms are commonly used for two purposes: 1) characterization of observed reflectance response to controlled optical properties within the phantom, and 2) calibration of the wavelength-specific reflectance device response to allow system independent interpretation of measurements made in samples with uncontrolled optical properties. The results presented in this study have implications for both of these uses. Device characterization studies may seek to establish or validate a relationship between observed reflectance and μ_s' [16–18]. However, the data presented in this study show that scattering PF can profoundly influence observed relationships between reflectance intensity and μ_s'. The data in Figs. 4 and 6 show that for reflectance measurements that sample dimensionless reduced scattering coefficients below empirically identified threshold values ($\mu_s' d_f = 10$ for single fiber devices and $\mu_s' \rho = 0.5$ for separate source detector devices) the collected reflectance intensities are sensitive to PF-effects. Reflectance measurements performed below these thresholds collect a substantial component of light that has undergone few, or single, scattering events, making the probability of collecting light in that regime (at least somewhat) dependent on the backscattering features of the scattering PF. These data indicate that a proportionality established between reflectance intensity and μ_s' in IL at a single wavelength will not hold at other wavelengths. Moreover, proportionalities are not directly extensible to another scattering medium that may contain an unknown wavelength-dependent PF, such as tissue.

IL optical phantoms are also commonly used for system calibration purposes [10]. While this approach can be valid, care must be taken to consider influences of the PF. As shown in Figs. 3 and 5, spectral remission features can depend strongly on the IL dilution of the phantom. It is possible to account for these features by characterizing the response of the investigated device to the moments of the PF. This can be investigated either by experimental measurements in another scattering medium with a controlled wavelength-dependent PF, such as a phantom constructed with polystyrene beads [42], or simulation, where variation of PF can be completely controlled. The experimental data for single fiber reflectance spectra in this study were calibrated with measurements in IL, by using a Monte Carlo analysis to convert the measured reflectance spectra to an absolute scale (in units of % of incident photons) [35], a conversion that accounts for the wavelength-dependent PF influence. Such a calibration becomes independent of IL$_p$. This approach to spectral analysis requires sufficient information to estimate PF effects; such information could be provided by spectral information measured at an additional length scale such as with multiple fiber diameters [34,35,41] or at multiple distances from the source [14,33], or spectral information measured with an angular resolution [43,44]. The use of IL as a calibration phantom without correction for PF-effects may introduce a substantial bias into quantitative estimates of scattering parameters, especially if applied to measurements in a sample of unknown optical properties, such as tissue.

This study identified an interesting difference in the relationship between reflectance intensity and μ_s' for device geometries that utilize a single fiber as a source and detector compared with a device that utilizes separate source and detector fibers. Reflectance intensity collected by single fiber devices shows a monotonically increasing response to increases in μ_s', as displayed in Fig. 4. In contrast, reflectance intensity collected by separate source detectors shows a nonlinear response that increases or decreases based on $\mu_s' \rho$, as shown in Fig. 6. These limiting behaviors can be intuitively explained. The single fiber geometry allows collection of light that has scattered an infinitesimally small distance into the medium prior to collection. Therefore, in the limit of highly scattering media, the single fiber reflectance device is no less likely to collect light in response to increased μ_s'. In contrast, the collection geometry with separate source and detector fibers has a geometrical minimum path that light must travel within the medium prior to collection. Therefore, in the limit of highly scattering

media, the collected signal will be attenuated in response to increases in μ_s'. These differences in the required light path travelled by light collected by either device leads to different threshold sensitivities to PF, which empirically are $\mu_s' d_f = 10$ and $\mu_s' \rho = 0.5$ for each device-type, respectively. This means that for single fiber measurements, the transport length, defined by the inverse of the reduced scattering coefficient, must be an order of magnitude greater than the collection length to be independent of PF effects. A device with separate source detectors is (in general) less sensitive to PF, with collection at locations up to half of the transport length showing insensitivity to PF. This threshold is expected to be dependent on the source and detector fiber diameters, which were fixed at 0.2 mm in the current study; the exact value of the threshold may vary for different fibers sizes. It should be noted that in IL phantoms constructed to mimic the range of μ_s' expected in tissue, in the range of [0.5-2.0] mm^{-1} [37], devices that collect with ρ as large as 1 mm can be influenced by PF effects. Moreover, inspection of the data in Figs. 5 and 6 show that measurements made in such phantoms with adjacent source and detector fibers (ρ = 0.2 mm) may contain a spectral signature that shows little to no wavelength-dependence on μ_s'.

While this study specifically investigates the spectral response of specific reflectance geometries, the findings are important for other measurement devices as well. This study characterized the response over a set range of geometrical perturbations to single fiber size and source-detector distance. This study does not perform a comprehensive evaluation of all possible geometrical configurations of fiber probes (e.g. all possible source and detector fiber sizes, inter-fiber distances, or numerical apertures). The results of this study are applicable to reflectance spectra measured by any probe configuration: the sampled transport regime will determine sensitivity to wavelength-dependent changes in PF. The results are also important for devices that sample reflectance at a single wavelength. In this case, care must be taken to correctly interpret the collected signal to avoid mischaracterizing the observed reflectance intensity as influenced exclusively by μ_s'. For example, the use of raw reflectance intensity at a single wavelength to correct fluorescence for the influence of optical properties will be problematic considering that μ_s' and PF will influence reflectance and fluorescence intensities differently [9]. Ongoing work will characterize the PF-specific influences of fluorescence correction algorithms.

5 Conclusions

This study investigates the influence of the wavelength-dependent scattering properties μ_s' and PF on spectral features of reflectance collected near the source location in IL optical phantoms. Experiments and simulations are used to characterize features in the 400-800 nm wavelength range from IL optical phantoms with IL$_p$ in the range 0.454-5.675%, which relates to a wide range of μ_s' = [0.3–8] mm^{-1}. Data were measured or simulated for reflectance geometries that 1) utilized a single fiber optic for both source and detector with the d_f = [0.2–1.0] mm, and 2) separate source and detector fibers with core to core separations in the range ρ = [0.2–2.0] mm. Results for both collection configurations showed a dependence of spectral scattering features on the transport regime sampled during measurement. PF-dependent effects were observed in reflectance spectra measured below a dimensionless threshold of $\mu_s' d_f = 10$ (i.e. ten transport lengths) for single fiber devices and $\mu_s' \rho = 0.5$ (i.e. half a transport length) for separate source detector devices. The results show the need to consider the influence of PF when using measurements of IL to either characterize or calibrate a reflectance device that collects light close to the source.